MATERIALS SCIENCE

Correlation-driven eightfold magnetic anisotropy in a two-dimensional oxide monolayer

Zhangzhang Cui[1,2], Alexander J. Grutter[3], Hua Zhou[4], Hui Cao[1,2,4], Yongqi Dong[1,4], Dustin A. Gilbert[3,5], Jingyuan Wang[6], Yi-Sheng Liu[7], Jiaji Ma[8], Zhenpeng Hu[9], Jinghua Guo[7], Jing Xia[6], Brian J. Kirby[3], Padraic Shafer[7], Elke Arenholz[7,10], Hanghui Chen[8,11,12]*, Xiaofang Zhai[1,2,13]*, Yalin Lu[1,2]

Engineering magnetic anisotropy in two-dimensional systems has enormous scientific and technological implications. The uniaxial anisotropy universally exhibited by two-dimensional magnets has only two stable spin directions, demanding 180° spin switching between states. We demonstrate a previously unobserved eightfold anisotropy in magnetic $SrRuO_3$ monolayers by inducing a spin reorientation in $(SrRuO_3)_1/(SrTiO_3)_N$ superlattices, in which the magnetic easy axis of Ru spins is transformed from uniaxial ⟨001⟩ direction ($N < 3$) to eightfold ⟨111⟩ directions ($N \geq 3$). This eightfold anisotropy enables 71° and 109° spin switching in $SrRuO_3$ monolayers, analogous to 71° and 109° polarization switching in ferroelectric $BiFeO_3$. First-principle calculations reveal that increasing the $SrTiO_3$ layer thickness induces an emergent correlation-driven orbital ordering, tuning spin-orbit interactions and reorienting the $SrRuO_3$ monolayer easy axis. Our work demonstrates that correlation effects can be exploited to substantially change spin-orbit interactions, stabilizing unprecedented properties in two-dimensional magnets and opening rich opportunities for low-power, multistate device applications.

INTRODUCTION

Recent years have seen intense interest in stabilizing and controlling magnetic ordering in two-dimensional (2D) systems (*1*–*9*), motivated by both the potential to unlock new fundamental physics and enable new high-density, low-power spintronic device paradigms. Engineering magnetic anisotropy (MA) in 2D systems plays a critical role in realizing these new functionalities but remains challenging because of the lack of accessible control parameters. Atomically precise complex oxide superlattices provide an ideal platform for the manipulation of MA in magnetic monolayers, as the correlated electron physics enables uniquely powerful handles through strong coupling between the electronic, spin, orbital, and lattice degrees of freedom. These handles allow deterministic control of the electronic and magnetic ground state, leading to exotic phenomena such as high-temperature superconductivity, colossal magnetoresistance (MR), 2D electron gases, etc. (*10*, *11*).

High-quality $(SrRuO_3)_1/(SrTiO_3)_N$ superlattices, in which each $SrRuO_3$ monolayer is separated by N unit cells of $SrTiO_3$, are an ideal model system in which to explore the interplay between electron correlation and MA. The MA of a $SrRuO_3$ monolayer originates from strong spin-orbit interactions. Atomic spin-orbit coupling (SOC) is proportional to Z^4 (where Z is atomic number) (*12*, *13*), so that a 4d transition metal such as Ru exhibits a larger SOC energy (about 100 meV) than 3d transition metals (*14*). Ru^{4+} in bulk $SrRuO_3$ nominally has four d-orbital electrons in a low-spin configuration, where three electrons occupy the majority spin channel, while the fourth electron resides in the minority spin channel with occupational degeneracy among the three Ru t_{2g} orbitals (*15*–*18*). In this work, we propose to use oxide superlattices to tune Ru orbital occupancy, which changes the SOC energy and induces a nontrivial new MA in $SrRuO_3$ monolayers.

RESULTS

Structural characterizations of $(SrRuO_3)_1/(SrTiO_3)_N$ superlattices

The $(SrRuO_3)_1/(SrTiO_3)_N$ superlattices are shown schematically in Fig. 1A and were fabricated by pulsed laser deposition (PLD) assisted with reflective high-energy electron diffraction (RHEED). X-ray diffraction (XRD) measurements in Fig. 1B reveal superlattice peaks corresponding to the designed periodicity. Layer-by-layer growth and atomically flat surfaces are observed by in situ RHEED and atomic force microscopy, respectively (fig. S1). The x-ray absorption near-edge structures (XANES) of Ru *K*-edges are measured, which demonstrate similar Ru valences in the superlattices (fig. S2). XRD reciprocal space maps around the (2 0 4) substrate peak are shown in Fig. 1C, demonstrating that all superlattices are coherently strained to the $SrTiO_3$ substrates. The average z-axis lattice constants $c_{average}$ are calibrated and shown in Fig. 1D. The ideal z-axis lattice constants calculated as $c_{ideal} = (N \times c_{STO} + c_{SRO})/(N + 1)$ are used to fit $c_{average}$, where c_{STO} and c_{SRO} represent that of $SrTiO_3$ (3.905 Å) and $SrRuO_3$ (3.984 Å), respectively. This comparison shows that, within experimental uncertainty, $c_{average}$ matches c_{ideal} across all

[1]Hefei National Laboratory for Physical Sciences at the Microscale, National Synchrotron Radiation Laboratory, University of Science and Technology of China, Hefei, Anhui 230026, China. [2]Synergetic Innovation Center of Quantum Information and Quantum Physics, University of Science and Technology of China, Hefei, Anhui 230026, China. [3]NIST Center for Neutron Research, National Institute of Standards and Technology, Gaithersburg, MD 20899, USA. [4]Advanced Photon Source, Argonne National Laboratory, Lemont, IL 60439, USA. [5]Department of Materials Science and Engineering, University of Tennessee, Knoxville, TN 37996, USA. [6]Department of Physics, University of California, Irvine, Irvine, CA 92697, USA. [7]Advanced Light Source, Lawrence Berkeley National Laboratory, Berkeley, CA 94720, USA. [8]NYU-ECNU Institute of Physics, NYU Shanghai, Shanghai 200122, China. [9]School of Physics, Nankai University, Tianjin 300071, China. [10]Cornell High Energy Synchrotron Source, Cornell University, Ithaca, NY 14853, USA. [11]State Key Laboratory of Precision Spectroscopy, School of Physical and Material Sciences, East China Normal University, Shanghai 200062, China. [12]Department of Physics, New York University, New York, NY 10027, USA. [13]School of Physical Science and Technology, ShanghaiTech University, Shanghai 201210, China.
*Corresponding author. Email: zhaixf@shanghaitech.edu.cn (X.Z.); hanghui.chen@nyu.edu (H.Ch.)

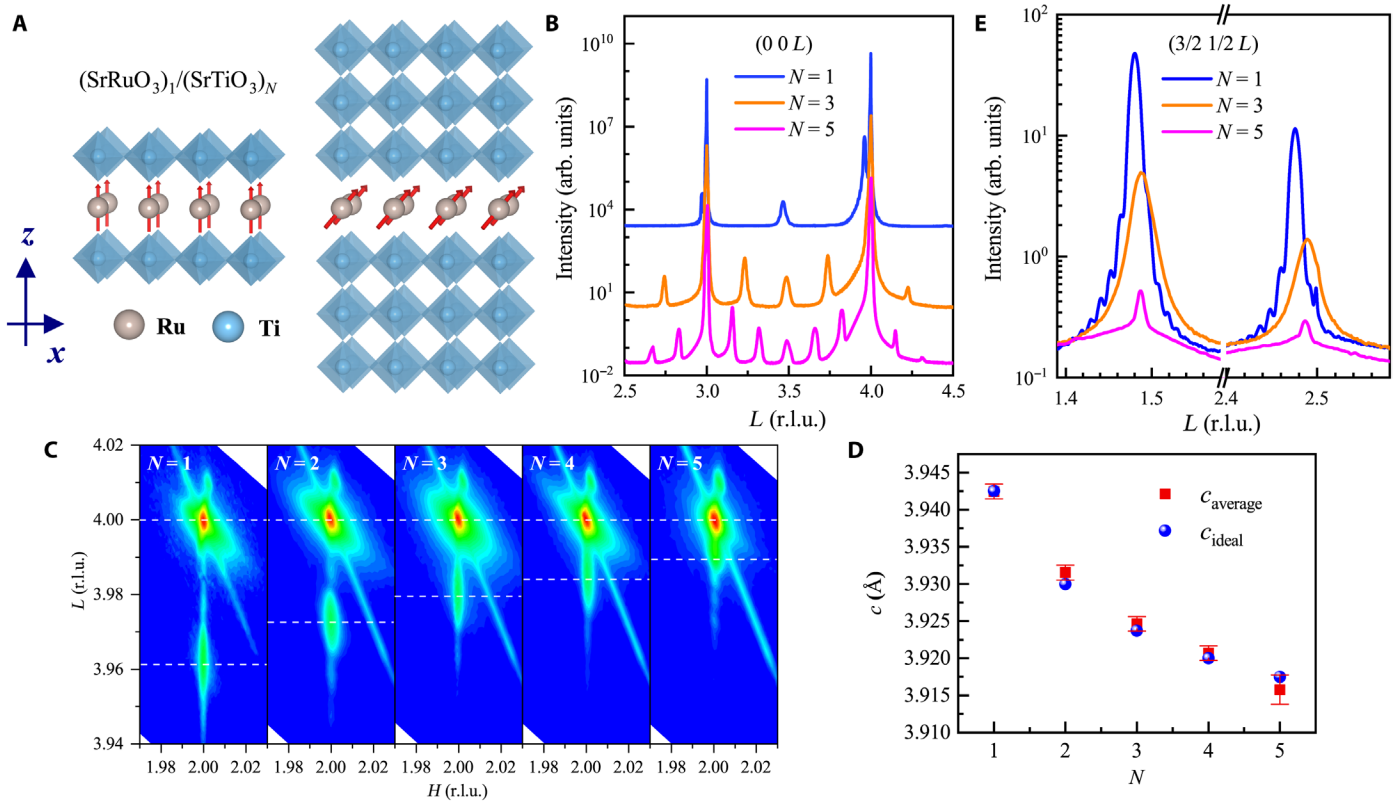

Fig. 1. Structural characterizations of $(SrRuO_3)_1/(SrTiO_3)_N$ superlattices. (**A**) Schematics of lattice structures of the $N = 1$ and $N = 3$ superlattices. (**B**) XRD ω-2θ scans of $N = 1$, 3, and 5 superlattices. (**C**) XRD reciprocal space maps of $N = 1$ to 5 superlattices taken around the (2 0 4) reflections of $SrTiO_3$ substrates. (**D**) Average and the ideal *c*-axis lattice constants of the superlattices. (**E**) The (3/2 1/2 *L*) half-order diffraction peaks of the $N = 1$, 3, and 5 superlattices. The reciprocal lattice units (r.l.u.) in (B), (C), and (E) are calculated using the $SrTiO_3$ substrate lattice. Error bars represent ±1 standard deviation.

N, so that the lattice constants and strain states of all superlattices are consistent.

Furthermore, we measured half-order diffraction peaks to reveal the oxygen octahedral rotation patterns (*19*–*21*). In all superlattices, $a^-a^-c^-$ rotation patterns are observed (see section S1 for details). Figure 1E shows the (3/2 1/2 3/2) and (3/2 1/2 5/2) half-order peaks with stronger intensities in superlattices of smaller *N*. In addition, extremely weak (*H*/2, *H*/2, *L*/2) diffraction peaks are observed in all superlattices (fig. S3, A and B), indicating that the residual a^- rotation is much smaller than the c^- rotation. We therefore conclude that all superlattices exhibit tetragonal structural symmetry with $a^-a^-c^-$ type octahedral rotations, where the c^- rotations are larger than the a^- rotations.

Magnetism and Curie temperatures of $(SrRuO_3)_1/(SrTiO_3)_N$ superlattices

In Fig. 2 (A and B), we show the Ti *L*-edge x-ray absorption spectroscopy (XAS) and x-ray magnetic circular dichroism (XMCD) of the superlattices measured at a temperature (*T*) of 10 K in an applied magnetic field (*H*) of 4 T. As the absorption energy of the Ru *M*-edge and Ti *L*-edge overlap, the XAS and XMCD are completely dominated by Ti so that it is not possible to distinguish the Ru *M*-edge signal in the superlattices (*22*). More XMCD data with both normal and grazing incidence beam of the other superlattices are shown in fig. S4. No measurable valence change or magnetic dichroism was observed on the Ti edge in all superlattices, excluding any magnetic contribution from the $SrTiO_3$ and indicating that the magnetization (*M*) is confined purely within the $SrRuO_3$ layers. The magnetism and MA of the $SrRuO_3$ monolayer are further revealed by superconducting quantum interference device (SQUID) magnetometer and magneto-optic Kerr effect (MOKE) measurements. The former detects the overall magnetism from the film and possible artificial backgrounds, while the latter only detects the film with an optical penetration depth (~30 nm) less than the film thickness. Note that the cooling fields to orient the magnetic domains are 0.05 and 0.5 T for the MOKE and SQUID measurements, respectively. The lower cooling field yielded the low-temperature peak features in some of the MOKE measurements. The temperature-dependent Kerr rotation (Fig. 2C, right axis, and fig. S5A) reveals Curie temperatures (T_C) of approximately 100 K for the $N = 1$ and 70 K for the $N = 2$ to 5 superlattices. Thus, the magnetic transition can be confirmed to be intrinsic to the films.

The quantitative magnetizations of the superlattices are studied using SQUID *M*–versus–*H* measurements (Fig. 2, D to F, and fig. S5, B and C), which reveals a saturation magnetization between 0.5 μ_B/Ru and 0.7 μ_B/Ru for the $N = 1$ and 2 superlattices and approximately 0.4 μ_B/Ru for the $N \geq 3$ superlattices. Interestingly, the MA of the superlattices exhibits a notable dependence on the $SrTiO_3$ layer number. The $N \leq 2$ superlattices are similar to the bulk, remaining uniaxial with the easy axis along [001] (see Fig. 2D and fig. S5B). However, the magnetic hysteresis of the $N \geq 3$ superlattices indicates the easy axis transition to be along the [111] direction [see Fig. 2 (E and F) and fig. S5C].

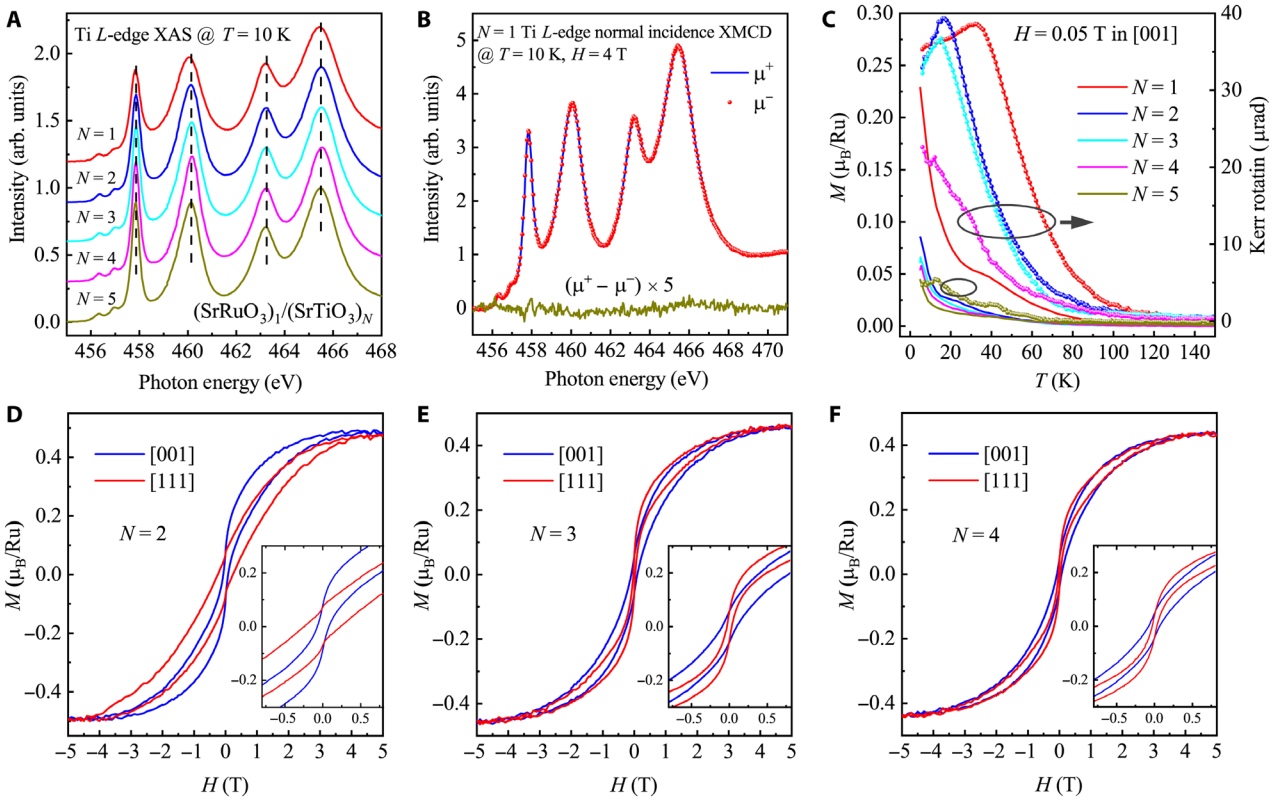

Fig. 2. XMCD and SQUID magnetic characterizations of $(SrRuO_3)_1/(SrTiO_3)_N$ superlattices. Ti *L*-edge (**A**) XAS and (**B**) XMCD of $N = 1$ to 5 superlattices. (**C**) SQUID magnetization (left axis) and MOKE Kerr rotation (right axis) measurements as a function of temperature of $N = 1$ to 5 superlattices. The measurements were taken during warming with 0.05-T field applied in the [001] direction. The magnetization versus magnetic field measured in the [001] and [111] directions of (**D**) $N = 2$, (**E**) $N = 3$, and (**F**) $N = 4$ superlattices at 5 K. The insets are the zoom-in view of the loops at low field.

Depth-dependent magnetization distribution

Since the Ru *M*-edge XMCD was not detectable, we have probed the magnetization distribution in the $N = 3$ superlattice with polarized neutron reflectometry (PNR), as shown in Fig. 3A. Although the superlattice repeat length is extremely thin, so that the first-order Bragg reflection appears at approximately 4 nm^{-1}, the extremely sharp interfaces and sample uniformity allow the observation of a clear superlattice peak in the expected location, as shown in Fig. 3B. Because the neutron spin provides sensitivity to the magnetic scattering length densities, analysis and model fitting of the PNR data allow a depth-dependent picture of the magnetization distribution to be extracted, shown in Fig. 3D. Specifically, we note that a nonzero splitting (see Fig. 3C) is observed between the (++) and (−−) reflectivities near the critical edge, which indicates an intrinsic net magnetization within the film of at least 0.24 μ_B/Ru and up to 0.37 μ_B/Ru. The PNR-detected magnetization is slightly smaller than the SQUID magnetization but agrees reasonably well given possible background contributions to the SQUID value. Furthermore, a small but statistically notable spin asymmetry (SA), defined as $(R^{++} - R^{--})/(R^{++} + R^{--})$, of 0.167 ± 0.045 was observed at the first-order Bragg reflection. Modeling indicates that the SA of this feature is highly dependent on which layer the net magnetization originates in, with magnetic $SrRuO_3$ yielding a positive SA and magnetic $SrTiO_3$ yielding a negative SA. Since the observed SA is clearly positive, we conclude with high confidence that the observed magnetism originates from the $SrRuO_3$ layers as expected. Model fitting of the data supports this interpretation, with an approximate fitted magnetic moment of $0.004\ \mu_B/Ti \pm 0.055\ \mu_B/Ti$ in the $SrTiO_3$ layers. We therefore conclude that PNR reveals net magnetization originating from the $SrRuO_3$ monolayers in excellent agreement with the SQUID, MOKE, and Ti XMCD measurements.

MA of $(SrRuO_3)_1/(SrTiO_3)_N$ superlattices

To reveal the exact symmetry of the MA, we perform transverse MR and magnetic field angle-dependent resistance (MAR) measurements. The MR was measured at 5 K with the current driven along the [100] direction (Fig. 4, A and B). The MR of $N = 1$ and 2 superlattices with magnetic field H // [001] shows a two-peak structure with lobes reflecting the magnetic hysteresis loops. In contrast, the hysteresis loops are suppressed in the MR with H // [010], consistent with the weaker in-plane magnetization of the $N = 1$ and 2 superlattices. The MR measurements of the $N = 3$ to 5 superlattices all show similar behavior in the H // [001] and H // [010] measurements, indicating symmetric in-plane and out-of-plane spin alignments. Figure 4C presents the polar plots of the MAR of $(SrRuO_3)_1/(SrTiO_3)_N$ superlattices measured at $H = 9$ T and at temperatures of 5, 25, and 50 K. The MAR of $N = 3$ and 5 superlattices with 5-K temperature steps are shown in fig. S6 (A and B). Here, we define MAR as $MAR = (\rho(\theta) - \rho(90°))/\rho(90°)$, where ρ is the resistivity and θ represents the angle between the magnetic field H and the film surface normal (see the inset of Fig. 4B). H was rotated in the (100) plane with the electric current maintained perpendicular to the field. The $N = 1$ and 2 samples

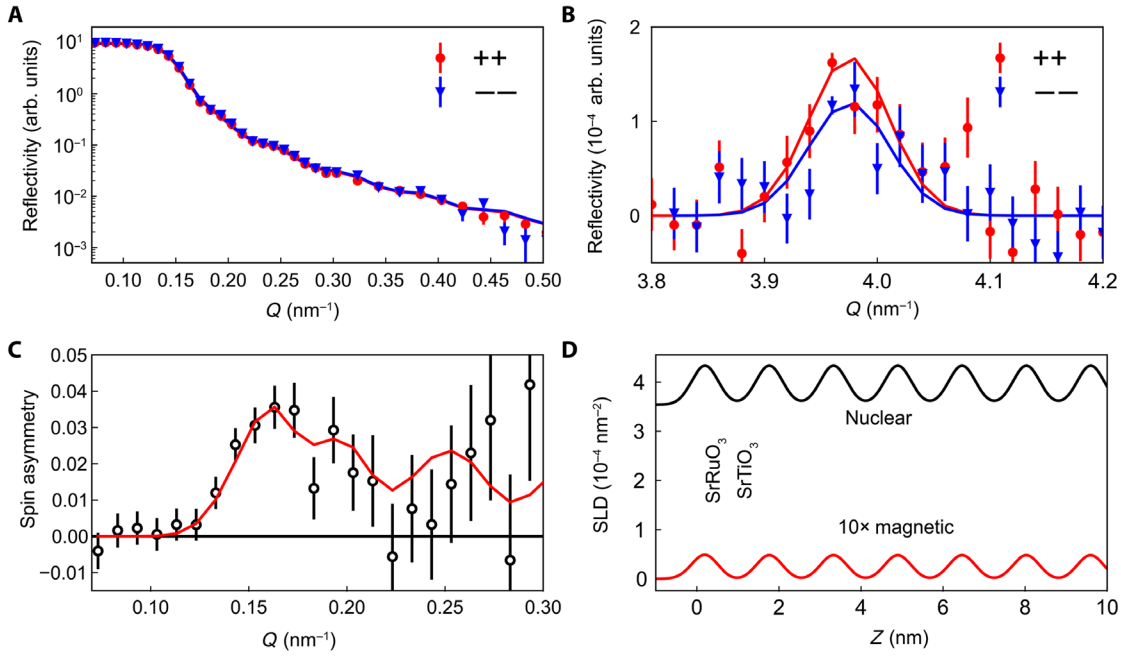

Fig. 3. PNR of a 50-repeat $(SrRuO_3)_1/(SrTiO_3)_3$ superlattice. (**A**) Fitted PNR data. (**B**) Superlattice Bragg reflection fitted with Gaussian peaks to demonstrate the difference in peak height. (**C**) SA near the critical edge showing clear spin-dependent splitting of the reflectivities. All measurements were performed at 6 K under an applied field of 3 T. (**D**) Representative section of the nuclear and magnetic scattering length density (SLD) profiles used to generate the fits shown in (A) and (C). Error bars represent ±1 standard deviation.

exhibit perpendicular MA at all measured temperatures, as do all other samples at $T > 25$ K, consistent with the perpendicular MA identified in the SQUID measurements. For $N \geq 3$, we observe a transition from twofold perpendicular MA to fourfold MA with decreasing temperature. The magnetic easy axes at low temperatures are along the [011], [0$\bar{1}$1], [01$\bar{1}$], and [0$\bar{1}\bar{1}$] directions. The MAR at 5 K with H rotating in the (010) and (001) planes is similar with that of the (100) plane (fig. S6, C and D), as expected given the pseudocubic structure of $SrRuO_3$ crystal lattice in the superlattices. More comprehensive MAR measurements at 5 K of the $N = 3$ superlattice with H rotating in the (110) plane (Fig. 4D) reveal an angle of ~71°/109° between the two magnetic easy axes within the (110) plane. Thus, the observed MAR symmetry identifies magnetic easy axes along the eightfold ⟨111⟩ directions of the $SrRuO_3$ pseudocubic lattice. These results confirm that perpendicular MA exists in $SrRuO_3$ monolayers for $N \leq 2$ superlattices at all temperatures and in $N \geq 3$ superlattices above ~25 K. Below approximately 25 K (±5 K), the $SrRuO_3$ monolayers in $N \geq 3$ superlattices exhibits eightfold MA.

First-principle calculations of the MA

To understand why MA of $(SrRuO_3)_1/(SrTiO_3)_N$ superlattices changes with the thickness of $SrTiO_3$ at low temperatures, we perform first-principle calculations. The in-plane lattice constants (along x and y axes) of all superlattices are constrained to match the theoretical lattice constant of the $SrTiO_3$ substrate. We start from a crystal structure with the experimentally observed $a^-a^-c^-$ rotation pattern (space group no. 14, $P2_1/c$). After atomic relaxation, density functional theory (DFT) calculations find a large rotation angle γ about the z axis but a very small rotation angle α about the x and y axes (≈ 0.5°) in both $N = 1$ and $N = 3$ superlattices, consistent with the XRD results. The layer-resolved rotation angles α and γ of each oxygen octahedron are shown in Fig. 5 (A and D). We note that the calculated γ angles from our calculations are very similar to those reported in a previous study (*5*).

Figure 5B shows the near–Fermi-level density of states (DOS) of the $N = 1$ superlattice. Ru in $SrRuO_3$ has a formal d^4 occupancy, with three electrons occupying the majority spin state (upper half of the panel) and the fourth electron in the minority spin state (lower half of the panel). The $SrRuO_3/SrTiO_3$ interfaces remove the degeneracy between Ru d_{xy} and $d_{xz/yz}$, so that the fourth (minority spin) electron is evenly shared by Ru d_{xz} and Ru d_{yz} orbitals. This electronic structure is consistent with previous results (*5*, *15*). Turning on SOC to induce MA, we test three different magnetic moment orientations: along ⟨001⟩, ⟨100⟩, and ⟨111⟩ directions. We find that in the $N = 1$ superlattice, the ⟨001⟩ state has the lowest total energy among the three magnetic orientations (Fig. 5C), in agreement with the SQUID and magnetotransport measurements. The twofold ⟨001⟩ MA is explicitly shown in the inset of Fig. 5C.

However, in the $N = 3$ superlattice, we find a completely new correlated state with different electronic, magnetic, and orbital properties. Figure 5E shows the near–Fermi-level DOS of the $N = 3$ superlattice, which indicates semiconducting behavior with a small bandgap of about 0.1 eV, in agreement with the transport measurements (fig. S7A). In the $N = 3$ superlattice, in the minority spin channel, Ru d_{xz} and Ru d_{yz} orbitals hybridize into a pair of new orbitals Ru $\alpha\,|\,xz\rangle + \beta\,|\,yz\rangle$ orbital [referred to as Ru (+) state] and Ru $\beta\,|\,xz\rangle - \alpha\,|\,yz\rangle$ orbital [referred to as Ru (−) state], where $\alpha^2 + \beta^2 = 1$. From our DFT + U calculations, we find $\alpha \sim \beta \sim 1/\sqrt{2}$. In each RuO_2 plane, there are two distinct Ru atoms: On one Ru atom, the fourth electron fills Ru (+) state and leaves Ru (−) state empty; on the other Ru atom, the fourth electron fills Ru (−) state and leaves Ru (+) state empty. The filled new orbital is referred to as a lower Hubbard band, which is just below the Fermi level; the empty new orbital is referred to as an upper Hubbard band, which is about 2 eV above the Fermi level. Such an

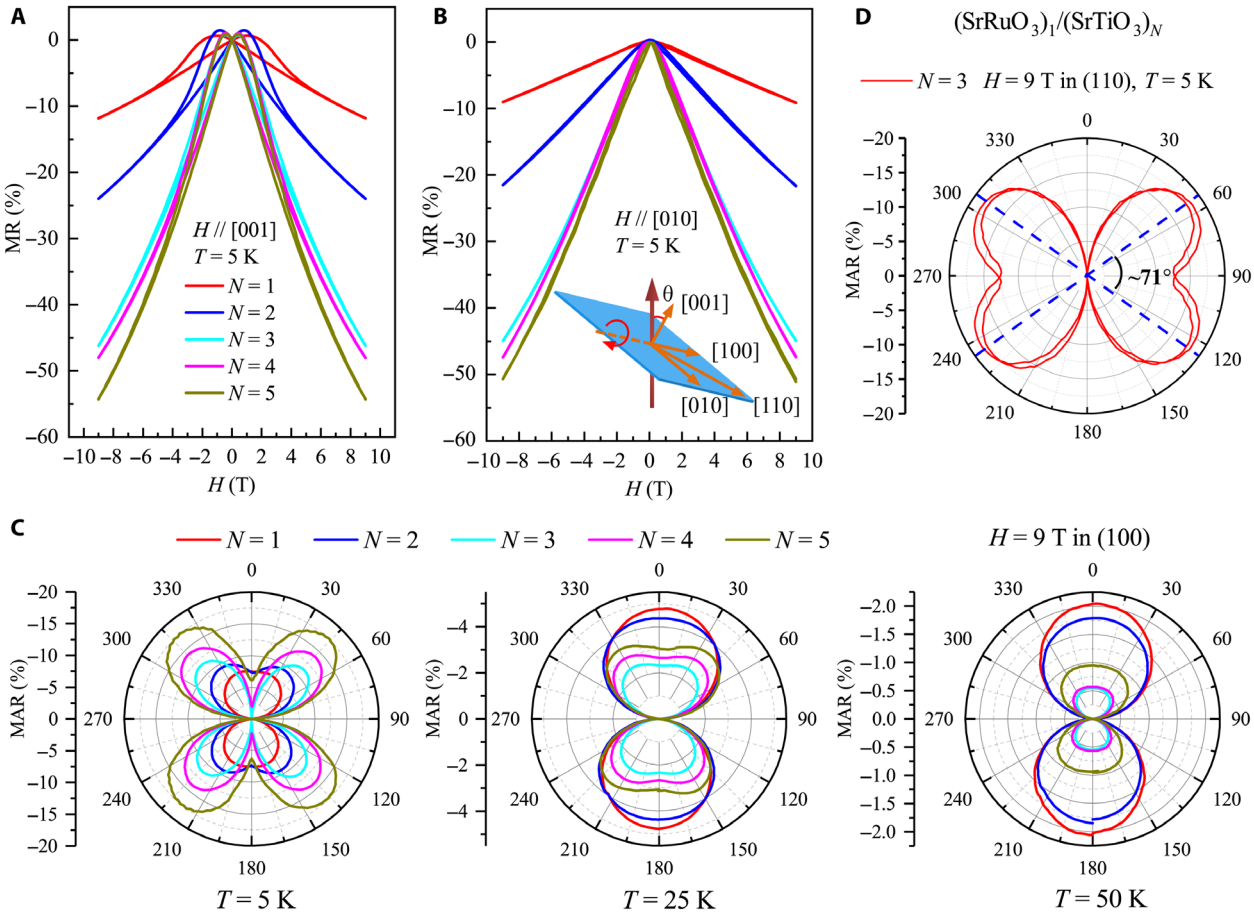

Fig. 4. Magnetotransport properties of $(SrRuO_3)_1/(SrTiO_3)_N$ superlattices. The MR at $T = 5$ K of $N = 1$ to 5 superlattices with the magnetic field applied parallel to (**A**) [001] and (**B**) [010] directions. The color correspondences are the same in (A) and (B). (**C**) Polar plots of MAR of $N = 1$ to 5 superlattices measured under a magnetic field of 9 T and at temperatures of 5, 25, and 50 K. The geometry of the MAR measurement is shown in the inset of (B). The sample rotates around the [100] direction, and the current is along the [100] direction, always being perpendicular to the magnetic field. θ is between the [001] direction and the field direction within the (100) plane. (**D**) Polar plots of MAR of $N = 3$ superlattice measured under a magnetic field of 9 T and at temperature of 5 K. The sample rotates around the [110] direction, and the current is along the [110] direction. θ is between the [001] direction and the field direction within the (110) plane. Both MAR with the sample rotating clockwise and anticlockwise are shown.

orbital ordering is very similar to what is found in layered perovskite K_2CuF_4, in which the hole orbitals $|x^2 - r^2\rangle$ and $|y^2 - r^2\rangle$ alternate in a basal plane (*23*). This orbital ordering results in a ferromagnetic insulating state in the CuF_2 plane according to Goodenough-Kanamori-Anderson rule (*24*–*26*). The emergence of the new orbital ordering in the $N = 3$ superlattice is corroborated with the fact that in each RuO_2 layer, Ru has one pair of long Ru-O bond and one pair of short Ru-O bond (2.06 and 1.97 Å, respectively) in our DFT calculation. Such a bond disproportionation has also been observed in our calculated results of $N = 5$ superlattice and in K_2CuF_4 (*23*). On the other hand, in the $N = 1$ superlattice in which the new orbital ordering does not occur, our calculation shows that Ru has four equal Ru-O bonds in the RuO_2 plane (2.00 Å).

It is precisely this new orbital ordering that changes MA. To demonstrate this, we turn on SOC and find that in the $N = 3$ superlattice, the ⟨001⟩ state does not have the lowest energy but rather, the ⟨111⟩ state becomes the most stable among the three magnetic orientations considered (Fig. 5F), which is consistent with the key experimental discovery as described above. The eightfold ⟨111⟩ MA is explicitly shown in the inset of Fig. 5F. The DFT calculation of $N = 5$ superlattice is similar to that of $N = 3$, and the results are shown in fig. S8. The reason a new correlated state emerges in the $N = 3$ and 5 superlattices is that with the RuO_2 layers further separated, interplanar Ru-Ru hopping is suppressed, decreasing the band width of Ru antibonding states (Fig. 5, B and E) and increasing correlation effects on the Ru sites. Furthermore, the rotations of oxygen octahedra reduce the crystal symmetry, contributing to the removal of the orbital degeneracy (fig. S9). The two factors combined lead to a hybridization of Ru d_{xz} and Ru d_{yz} orbitals and a split into a pair of lower and upper Hubbard bands. The role of oxygen octahedral tilts on the electronic structure is discussed in section S2. The new correlation-driven orbital ordering and the resulting eightfold ⟨111⟩ MA of $(SrRuO_3)_1/(SrTiO_3)_N$ ($N \geq 3$) superlattices are different from those of magnetic interfaces in previous studies (*27*–*31*).

DISCUSSION

Our study reveals a novel eightfold ⟨111⟩ MA in $SrRuO_3$ monolayers in $(SrRuO_3)_1/(SrTiO_3)_N$ superlattices ($N \geq 3$). Theoretically, our first-principle calculations demonstrate that the enhanced correlation

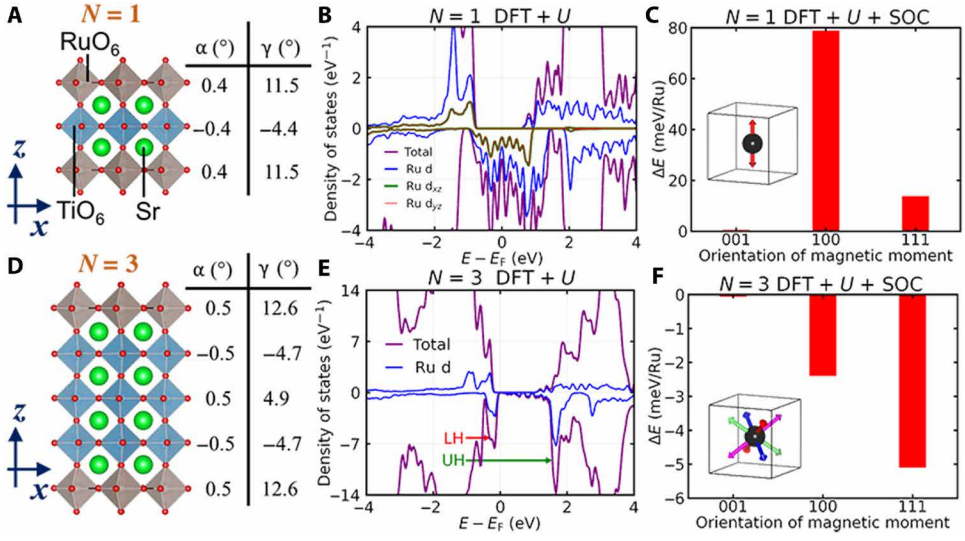

Fig. 5. DFT calculated crystal structure, DOS, and MA of $(SrRuO_3)_1/(SrTiO_3)_N$ superlattices. Crystal structures of (**A**) $N = 1$ and (**D**) $N = 3$ superlattices. Near–Fermi-level DOS of (**B**) $N = 1$ and (**E**) $N = 3$ superlattices, calculated using DFT + U method with $U_{Ru} = 4$ eV. The states in the upper (lower) half correspond to spin up (down). In (E), "LH" ("UH") means a lower (upper) Hubbard band, which is filled (empty). Because of the orbital ordering described in the main text, in each RuO_2 plane, there are two distinct Ru atoms (labeled as Ru1 and Ru2): For Ru1, LH is Ru (−) orbital, and UH is Ru (+); for Ru2, LH is Ru (+) orbital, and UH is Ru (−) orbital. The definition of Ru (+) and Ru (−) orbitals can be found in the main text. Total energy of (**C**) $N = 1$ and (**F**) $N = 3$ superlattices with different magnetic moment orientations, calculated using DFT + U + SOC method with $U_{Ru} = 4$ eV. ⟨001⟩, ⟨100⟩, and ⟨111⟩ refer to the orientation of Ru magnetic moments. The energy of the ⟨001⟩ state is used as the reference. The twofold ⟨001⟩ MA is explicitly shown in the inset of (C). The eightfold ⟨111⟩ MA is explicitly shown in the inset of (F).

strength on Ru atoms leads to a metal-to-semiconductor transition and induces an orbital ordering that is different from that of $N = 1$ superlattice but is similar to ferromagnetic insulator K_2CuF_4. The emergent orbital ordering changes the underlying spin-orbit interaction, reorienting the Ru magnetic easy axis. Experimentally, we performed four independent measurements (SQUID, MOKE, PNR, and MR) to understand the magnetic property of $(SrRuO_3)_1/(SrTiO_3)_N$ superlattices. First, we find that paramagnetism is unlikely because we observe hysteresis loops in both SQUID and transverse MR measurements, which is the characteristic feature of ferromagnetic materials. In addition, the temperature dependence of the Kerr rotation is incompatible with the usual Curie-Weiss behavior of paramagnetism. Second, the saturation magnetization around 0.3 μ_B/Ru in $N \geq 3$ superlattices is much larger than the usual net moment of canted antiferromagnetism in complex oxides (*32*–*35*). Furthermore, the reasonable agreement between the saturation magnetizations measured by PNR and SQUID does not support the possibility of an unintentionally subtracted linear M-versus-H dependence, which is the fingerprint proof of canted antiferromagnetism (*35*–*38*). On the other hand, ferromagnetism with a relatively small saturation moment is compatible with all the results that we have obtained, and we consider it as the most likely magnetic property in the large N superlattices.

Our work demonstrates that tuning interlayer electron hopping via digital oxide superlattices is a powerful tool for controlling spin-orbit interaction in solids and inducing novel physical properties in 2D magnetic monolayers, which are not exhibited by their bulk counterparts. MA with symmetry higher than fourfold is extremely rare in bulk magnetic materials, let alone 2D magnetic monolayers. The new eightfold ⟨111⟩ MA in a magnetic monolayer has far-reaching scientific and technological implications, such as multistate memory devices with eight degenerate magnetic states in real space, spin-transfer or spin-orbit torque with a minimum of 71° spin switching (which will substantially reduce the critical current), and control of topological spin textures when inversion symmetry is broken (*39*–*41*).

MATERIALS AND METHODS

Preparation and structural characterizations of $(SrRuO_3)_1/(SrTiO_3)_N$ superlattices

The $(SrRuO_3)_1/(SrTiO_3)_N$ ($N = 1$ to 5) superlattices were fabricated on (001) $SrTiO_3$ substrates using single-crystalline $SrTiO_3$ and ceramic $SrRuO_3$ targets by PLD assisted with RHEED. $SrTiO_3$ substrates with atomically flat TiO_2 termination were obtained via buffered hydrofluoric acid etching and annealing. The RHEED system was used to monitor the layer-by-layer growth of the films, and the total repetitions of the $N = 1$ to 5 superlattices are all 50. The thicknesses of both the $SrRuO_3$ layer and the $SrTiO_3$ layer are precisely controlled at a single molecular level by RHEED. All films were grown at a substrate temperature around 700°C and under an oxygen pressure of 10 Pa. During the growth, the laser frequency and energy density were 2 Hz and ~1 J/cm^2, respectively. After the deposition, all films were in situ annealed at 500°C for an hour in an oxygen environment of 5×10^4 Pa to remove oxygen vacancies. Synchrotron XRD measurements were conducted at the Advanced Photon Source, Argonne National Laboratory on beamline 12-ID-D using the Pilatus 100K detector and at the Shanghai Synchrotron Radiation Facility on beamline 14B.

Magnetic and magnetotransport characterizations

The magnetic properties of the superlattices were probed using SQUID and MOKE techniques. The temperature-dependent magnetization and Kerr rotation measurements of the superlattices were done during warming up under a smaller field of 0.05 T after the samples were

first cooled down to 4 K under a field of 0.5 T for SQUID and 0.05 T for MOKE. The transport properties were measured using a standard linear four-probe method by a physical property measurement system equipped with a sample rotator. Au electrodes were deposited using Ar ion sputtering on top of the superlattices. During the transport measurements, the dc current of around 10 μA was applied to the films, and the direction of the current was maintained to be perpendicular to the magnetic field.

PNR measurements

PNR measurements were performed using the polarized beam reflectometer instrument at the National Institute of Standards and Technology Center for Neutron Research. Samples were cooled to 6 K in an applied field of 3 T. Full polarization analysis was performed using both a spin polarizer and spin analyzer. The spin-dependent reflectivity was measured as a function of the scattering vector Q along the film normal. Data were reduced with the Reductus software package (*42*) and analyzed with the Refl1D software package for reflectometry modeling (*43*). Uncertainties in fitted parameters were extracted using a Markov chain Monte Carlo algorithm Differential Evolution Adaptive Metropolis (DREAM) as implemented in the Bumps python package. We note that PNR is sensitive only to the net in-plane components of the magnetization within the film, so that any out-of-plane component, for example, canted toward <111> axes will not be observed. For that reason, the reported magnetization values have been adjusted to account for the fact that SQUID magnetometry indicates that the films are approximately 10% below saturation value at 3 T. We also note that since no in-plane perpendicular magnetization component is expected in an applied field of 3 T, the spin-flip reflectivities R^{+-} and R^{-+} are expected to be zero and were not collected. Only the non-spin-flip scattering cross sections R^{++} and R^{--} were measured.

X-ray spectroscopic measurements

The Ti *L*-edge XAS and XMCD measurements were performed on beamline 4.0.2 at the Advanced Light Source (ALS) of Lawrence Berkeley National Laboratory at a temperature of 10 K and under the vacuum pressure of ($\approx$ or <) 1×10^{-6} Pa. The XAS spectra were recorded in total electron yield (TEY) mode (sample-to-ground drain current) and normalized by the incident photon flux determined from the photocurrent of an upstream Au mesh. The samples were measured with alternating left-polarized (μ^+) and right-polarized (μ^-) photons at 10 K cooled by liquid helium in an applied field of 4 T. During the XMCD measurement, the incident beam was perpendicular or inclined with a grazing angle of 20° to the sample surface and the spectra were collected in both TEY and luminescence yield mode. Preliminary room temperature XAS measurements have been performed on beamline 8.0.1 at ALS and beamline BL12B-a at the National Synchrotron Radiation Laboratory of China. The XANES measurements at Ru *K*-edge were performed at the beamline 12-BM-B, and the x-ray linear dichroism measurements at Ru L_3-edge were carried out at the beamline 4-ID-D at the Advanced Photon Source of Argonne National Laboratory.

First-principle calculations

We perform DFT calculations using a plane wave basis set and projector-augmented wave method (*44*), as implemented in the Vienna Ab initio Simulation Package (*45*). We use Perdew-Burke-Ernzerhof (PBE) generalized gradient approximation as exchange correlation functional (*46*). An energy cutoff of 600 eV is used throughout the calculations. The Brillouin zone integration is performed with a Gaussian smearing of 0.05 eV over a Γ-centered *k*-mesh of $12 \times 12 \times 12$ for the $N = 1$ superlattice and a Γ-centered *k*-mesh of $12 \times 12 \times 6$ for the $N = 3$ and 5 superlattices. The threshold of self-consistent calculations is 10^{-6} eV. Crystal structure is relaxed until each force component is smaller than 0.01 eV/Å. The in-plane lattice constant is fixed to be 3.93 Å, which is the theoretical lattice constant of $SrTiO_3$ calculated by DFT-PBE method. Correlation effects on Ru atoms are taken into account (*47*) by using the rotationally invariant Hubbard *U* method in DFT calculations (DFT + *U* method) (*48*). Following the previous study, we use $U_{Ru} = 4$ eV (*5*). The key results do not qualitatively change for $U_{Ru} \geq 3$ eV. SOC is turned on to study MA in DFT + *U* + SOC calculations.

SUPPLEMENTARY MATERIALS

Supplementary material for this article is available at http://advances.sciencemag.org/cgi/content/full/6/15/eaay0114/DC1

REFERENCES AND NOTES

1. A. J. M. Giesbers, K. Uhlířová, M. Konečný, E. C. Peters, M. Burghard, J. Aarts, C. F. J. Flipse, Interface-induced room-temperature ferromagnetism in hydrogenated epitaxial graphene. *Phys. Rev. Lett.* **111**, 166101 (2013).
2. B. Huang, G. Clark, E. Navarro-Moratalla, D. R. Klein, R. Cheng, K. L. Seyler, D. Zhong, E. Schmidgall, M. A. McGuire, D. H. Cobden, W. Yao, D. Xiao, P. Jarillo-Herrero, X. Xu, Layer-dependent ferromagnetism in a van der Waals crystal down to the monolayer limit. *Nature* **546**, 270–273 (2017).
3. J. A. Bert, B. Kalisky, C. Bell, M. Kim, Y. Hikita, H. Y. Hwang, K. A. Moler, Direct imaging of the coexistence of ferromagnetism and superconductivity at the $LaAlO_3/SrTiO_3$ interface. *Nat. Phys.* **7**, 767–771 (2011).
4. L. Li, C. Richter, J. Mannhart, R. C. Ashoori, Coexistence of magnetic order and two-dimensional superconductivity at $LaAlO_3/SrTiO_3$ interfaces. *Nat. Phys.* **7**, 762–766 (2011).
5. M. Verissimo-Alves, P. García-Fernández, D. I. Bilc, P. Ghosez, J. Junquera, Highly confined spin-polarized two-dimensional electron gas in $SrTiO_3/SrRuO_3$ superlattices. *Phys. Rev. Lett.* **108**, 107003 (2012).
6. A. J. Grutter, H. Yang, B. J. Kirby, M. R. Fitzsimmons, J. A. Aguiar, N. D. Browning, C. A. Jenkins, E. Arenholz, V. V. Mehta, U. S. Alaan, Y. Suzuki, Interfacial ferromagnetism in $LaNiO_3/CaMnO_3$ superlattices. *Phys. Rev. Lett.* **111**, 087202 (2013).
7. L. Hao, D. Meyers, H. Suwa, J. Yang, C. Frederick, T. R. Dasa, G. Fabbris, L. Horak, D. Kriegner, Y. Choi, J.-W. Kim, D. Haskel, P. J. Ryan, H. Xu, C. D. Batista, M. P. M. Dean, J. Liu, Giant magnetic response of a two-dimensional antiferromagnet. *Nat. Phys.* **14**, 806–810 (2018).
8. H. Boschker, T. Harada, T. Asaba, R. Ashoori, A. V. Boris, H. Hilgenkamp, C. R. Hughes, M. E. Holtz, L. Li, D. A. Muller, H. Nair, P. Reith, X. Renshaw Wang, D. G. Schlom, A. Soukiassian, J. Mannhart, Ferromagnetism and conductivity in atomically thin $SrRuO_3$. *Phys. Rev. X* **9**, 011027 (2019).
9. D. V. Christensen, Y. Frenkel, Y. Z. Chen, Y. W. Xie, Z. Y. Chen, Y. Hikita, A. Smith, L. Klein, H. Y. Hwang, N. Pryds, B. Kalisky, Strain-tunable magnetism at oxide domain walls. *Nat. Phys.* **15**, 269–274 (2019).
10. M. Imada, A. Fujimori, Y. Tokura, Metal-insulator transitions. *Rev. Mod. Phys.* **70**, 1039–1263 (1998).
11. H. Y. Hwang, Y. Iwasa, M. Kawasaki, B. Keimer, N. Nagaosa, Y. Tokura, Emergent phenomena at oxide interfaces. *Nat. Mater.* **11**, 103–113 (2012).
12. K. V. Shanavas, Z. S. Popović, S. Satpathy, Theoretical model for Rashba spin-orbit interaction in ***d*** electrons. *Phys. Rev. B* **90**, 165108 (2014).
13. S. Gariglio, A. D. Caviglia, J.-M. Triscone, M. Gabay, A spin–orbit playground: Surfaces and interfaces of transition metal oxides. *Rep. Prog. Phys.* **82**, 012501 (2018).
14. G. Cao, P. Schlottmann, The challenge of spin–Orbit-tuned ground states in iridates: A key issues review. *Rep. Prog. Phys.* **81**, 042502 (2018).
15. M. Gu, Q. Xie, X. Shen, R. Xie, J. Wang, G. Tang, D. Wu, G. P. Zhang, X. S. Wu, Magnetic ordering and structural phase transitions in a strained ultrathin $SrRuO_3/SrTiO_3$ superlattice. *Phys. Rev. Lett.* **109**, 157003 (2012).
16. Y. J. Chang, C. H. Kim, S.-H. Phark, Y. S. Kim, J. Yu, T. W. Noh, Fundamental thickness limit of itinerant ferromagnetic $SrRuO_3$ thin films. *Phys. Rev. Lett.* **103**, 057201 (2009).
17. J. Xia, W. Siemons, G. Koster, M. R. Beasley, A. Kapitulnik, Critical thickness for itinerant ferromagnetism in ultrathin films of $SrRuO_3$. *Phys. Rev. B* **79**, 140407 (2009).

18. D. E. Shai, C. Adamo, D. W. Shen, C. M. Brooks, J. W. Harter, E. J. Monkman, B. Burganov, D. G. Schlom, K. M. Shen, Quasiparticle mass enhancement and temperature dependence of the electronic structure of ferromagnetic $SrRuO_3$ thin films. *Phys. Rev. Lett.* **110**, 087004 (2013).
19. S. J. May, J.-W. Kim, J. M. Rondinelli, E. Karapetrova, N. A. Spaldin, A. Bhattacharya, P. J. Ryan, Quantifying octahedral rotations in strained perovskite oxide films. *Phys. Rev. B* **82**, 014110 (2010).
20. J. M. Rondinelli, S. J. May, J. W. Freeland, Control of octahedral connectivity in perovskite oxide heterostructures: An emerging route to multifunctional materials discovery. *MRS Bull.* **37**, 261–270 (2012).
21. X. Zhai, L. Cheng, Y. Liu, C. M. Schlepütz, S. Dong, H. Li, X. Zhang, S. Chu, L. Zheng, J. Zhang, A. Zhao, H. Hong, A. Bhattacharya, J. N. Eckstein, C. Zeng, Correlating interfacial octahedral rotations with magnetism in $(LaMnO_{3+\delta})_N/(SrTiO_3)_N$ superlattices. *Nat. Commun.* **5**, 4283 (2014).
22. K. Ishigami, K. Yoshimatsu, D. Toyota, M. Takizawa, T. Yoshida, G. Shibata, T. Harano, Y. Takahashi, T. Kadono, V. K. Verma, V. R. Singh, Y. Takeda, T. Okane, Y. Saitoh, H. Yamagami, T. Koide, M. Oshima, H. Kumigashira, A. Fujimori, Thickness-dependent magnetic properties and strain-induced orbital magnetic moment in $SrRuO_3$ thin films. *Phys. Rev. B* **92**, 064402 (2015).
23. D. I. Khomskii, G. A. Sawatzky, Interplay between spin, charge and orbital degrees of freedom in magnetic oxides. *Solid State Commun.* **102**, 87–99 (1997).
24. P. W. Anderson, Antiferromagnetism. Theory of superexchange interaction. *Phys. Rev.* **79**, 350–356 (1950).
25. J. B. Goodenough, Theory of the role of covalence in the perovskite-type manganites [La, *M*(II)] Mn O_3. *Phys. Rev.* **100**, 564–573 (1955).
26. J. Kanamori, Superexchange interaction and symmetry properties of electron orbitals. *J. Phys. Chem. Solid* **10**, 87–98 (1959).
27. D. Kan, R. Aso, R. Sato, M. Haruta, H. Kurata, Y. Shimakawa, Tuning magnetic anisotropy by interfacially engineering the oxygen coordination environment in a transition metal oxide. *Nat. Mater.* **15**, 432–437 (2016).
28. Z. Liao, M. Huijben, Z. Zhong, N. Gauquelin, S. Macke, R. J. Green, S. Van Aert, J. Verbeeck, G. Van Tendeloo, K. Held, G. A. Sawatzky, G. Koster, G. Rijnders, Controlled lateral anisotropy in correlated manganite heterostructures by interface-engineered oxygen octahedral coupling. *Nat. Mater.* **15**, 425–431 (2016).
29. D. Yi, J. Liu, S.-L. Hsu, L. Zhang, Y. Choi, J.-W. Kim, Z. Chen, J. D. Clarkson, C. R. Serrao, E. Arenholz, P. J. Ryan, H. Xu, R. J. Birgeneau, R. Ramesh, Atomic-scale control of magnetic anisotropy via novel spin-orbit coupling effect in $La_{2/3}Sr_{1/3}MnO_3/SrIrO_3$ superlattices. *Proc. Natl. Acad. Sci. U.S.A.* **113**, 6397–6402 (2016).
30. D. Yi, C. L. Flint, P. P. Balakrishnan, K. Mahalingam, B. Urwin, A. Vailionis, A. T. N'Diaye, P. Shafer, E. Arenholz, Y. Choi, K. H. Stone, J.-H. Chu, B. M. Howe, J. Liu, I. R. Fisher, Y. Suzuki, Tuning perpendicular magnetic anisotropy by oxygen octahedral rotations in $(La_{1-x}Sr_xMnO_3)/(SrIrO_3)$ superlattices. *Phys. Rev. Lett.* **119**, 077201 (2017).
31. L. Vistoli, W. Wang, A. Sander, Q. Zhu, B. Casals, R. Cichelero, A. Barthélémy, S. Fusil, G. Herranz, S. Valencia, R. Abrudan, E. Weschke, K. Nakazawa, H. Kohno, J. Santamaria, W. Wu, V. Garcia, M. Bibes, Giant topological hall effect in correlated oxide thin films. *Nat. Phys.* **15**, 67–72 (2019).
32. J. Matsuno, K. Ihara, S. Yamamura, H. Wadati, K. Ishii, V. V. Shankar, H.-Y. Kee, H. Takagi, Engineering a spin-orbital magnetic insulator by tailoring superlattices. *Phys. Rev. Lett.* **114**, 247209 (2015).
33. B. J. Kim, H. Ohsumi, T. Komesu, S. Sakai, T. Morita, H. Takagi, T. Arima, Phase-sensitive observation of a spin-orbital Mott state in Sr_2IrO_4. *Science* **323**, 1329–1332 (2009).
34. M. Ramazanoglu, M. Laver, W. Ratcliff II, S. M. Watson, W. C. Chen, A. Jackson, K. Kothapalli, S. Lee, S.-W. Cheong, V. Kiryukhin, Local weak ferromagnetism in single-crystalline ferroelectric $BiFeO_3$. *Phys. Rev. Lett.* **107**, 207206 (2011).
35. V. Skumryev, F. Ott, J. M. D. Coey, A. Anane, J.-P. Renard, L. Pinsard-Gaudart, A. Revcolevschi, Weak ferromagnetism in $LaMnO_3$. *Eur. Phys. J. B.* **11**, 401–406 (1999).
36. J. Geck, B. Büchner, M. Hücker, R. Klingeler, R. Gross, L. Pinsard-Gaudart, A. Revcolevschi, Evidence for canted antiferromagnetism in lightly doped $La_{1-x}Sr_xMnO_3$. *Phys. Rev. B* **64**, 144430 (2001).
37. I. E. Dzialoshinskii, Thermodynamic theory of "weak" ferromagnetism in antiferromagnetic substances. *J. Exp. Theor. Phys.* **5**, 1259–1272 (1957).
38. P.-G. de Gennes, Effects of double exchange in magnetic crystals. *Phys. Rev.* **118**, 141–154 (1960).
39. J. Matsuno, N. Ogawa, K. Yasuda, F. Kagawa, W. Koshibae, N. Nagaosa, Y. Tokura, M. Kawasaki, Interface-driven topological Hall effect in $SrRuO_3$-$SrIrO_3$ bilayer. *Sci. Adv.* **2**, e1600304 (2016).
40. M. Hepting, R. J. Green, Z. Zhong, M. Bluschke, Y. E. Suyolcu, S. Macke, A. Frano, S. Catalano, M. Gibert, R. Sutarto, F. He, G. Cristiani, G. Logvenov, Y. Wang, P. A. van Aken, P. Hansmann, M. Le Tacon, J.-M. Triscone, G. A. Sawatzky, B. Keimer, E. Benckiser, Complex magnetic order in nickelate slabs. *Nat. Phys.* **14**, 1097–1102 (2018).
41. L. Wang, Q. Feng, Y. Kim, R. Kim, K. H. Lee, S. D. Pollard, Y. J. Shin, H. Zhou, W. Peng, D. Lee, W. Meng, H. Yang, J. H. Han, M. Kim, Q. Lu, T. W. Noh, Ferroelectrically tunable magnetic skyrmions in ultrathin oxide heterostructures. *Nat. Mater.* **17**, 1087–1094 (2018).
42. B. Maranville, W. Ratcliff II, P. Kienzle, Reductus: A stateless python data reduction service with a browser front end. *J. Appl. Cryst.* **51**, 1500–1506 (2018).
43. B. J. Kirby, P. A. Kienzle, B. B. Maranville, N. F. Berk, J. Krycka, F. Heinrich, C. F. Majkrzak, Phase-sensitive specular neutron reflectometry for imaging the nanometer scale composition depth profile of thin-film materials. *Curr. Opin. Colloid Interface Sci.* **17**, 44–53 (2012).
44. P. E. Blöchl, Projector augmented-wave method. *Phys. Rev. B* **50**, 17953–17979 (1994).
45. G. Kresse, J. Furthmüller, Efficiency of ab-initio total energy calculations for metals and semiconductors using a plane-wave basis set. *Comp. Mater. Sci.* **6**, 15–50 (1996).
46. J. P. Perdew, K. Burke, M. Ernzerhof, Generalized gradient approximation made simple. *Phys. Rev. Lett.* **77**, 3865–3868 (1996).
47. H. Chen, Magnetically driven orbital-selective insulator–metal transition in double perovskite oxides. *npj Quantum Mater.* **3**, 57 (2018).
48. S. L. Dudarev, G. A. Botton, S. Y. Savrasov, C. J. Humphreys, A. P. Sutton, Electron-energy-loss spectra and the structural stability of nickel oxide: An LSDA + U study. *Phys. Rev. B* **57**, 1505–1509 (1998).
49. S. J. May, C. R. Smith, J.-W. Kim, E. Karapetrova, A. Bhattacharya, P. J. Ryan, Control of octahedral rotations in $(LaNiO_3)_n/(SrMnO_3)_m$ superlattices. *Phys. Rev. B* **83**, 153411 (2011).

Acknowledgments: We thank D. Schlom, Y. Suzuki, A. Millis, L. Li, and D. Yi for helpful discussions and C.-L. Dong and Y. Choi for extensive beamline supports. **Funding:** This work was supported by the National Key Research and Development Program of China (grant no. 2016YFA0401004) and the National Natural Science Foundation of China (grant nos. 51627901 and 11574287). The ALS is supported by the Director of the U.S. Department of Energy Office of Science, Office of Basic Energy Sciences, under contract no. DE-AC02-05CH11231. The Advanced Photon Source, a U.S. Department of Energy Office of Science user facility, is operated by Argonne National Laboratory under contract no. DE-AC02-06CH11357. Sagnac measurement at UC Irvine was supported by NSF grant DMR-180781. X.Z. acknowledges the support of the Youth Innovation Promotion Association CAS (grant no. 2016389). H.Ch. acknowledges the funding of the National Natural Science Foundation of China (grant no. 11774236), Shanghai Pujiang Talents Program (grant no. 17PJ1407300), Seed grant of NYU-ECNU Research Institute of Physics, and NYU University Research Challenge Fund. Computational resources are provided by NYU HPC resources at the New York campus, Abu Dhabi, and Shanghai. Certain commercial equipment is identified in this paper to foster understanding. Such identification does not imply recommendation or endorsement by the National Institute of Standards and Technology, nor does it imply that the materials or equipment identified are necessarily the best available for the purpose. **Author contributions:** X.Z. and Z.C. designed the project. Y.L. supervised the work done in USTC. Z.C. fabricated the samples and performed the magnetic and transport measurements. H.Ch. and J.M. performed the theoretical calculations. A.J.G., B.J.K., D.A.G., P.S., and E.A. performed the low-temperature XAS, XMCD, and PNR measurements. H.Ca., Y.D., and H.Z. performed the synchrotron XRD, Ru *K*-edge XANES, and Ru L_3-edge x-ray linear dichroism (XLD) experiments. J.W. and J.X. performed the MOKE measurement. X.Z., H.Ch., Z.C., and A.J.G. wrote the paper. All authors discussed the experimental data and commented on the manuscript writing. **Competing interests:** The authors declare that they have no competing interests. **Data and materials availability:** All data needed to evaluate the conclusions in the paper are present in the paper and/or the Supplementary Materials. Additional data related to this paper may be requested from the authors.

Submitted 12 May 2019
Accepted 13 January 2020
Published 10 April 2020
10.1126/sciadv.aay0114

Citation: Z. Cui, A. J. Grutter, H. Zhou, H. Cao, Y. Dong, D. A. Gilbert, J. Wang, Y.-S. Liu, J. Ma, Z. Hu, J. Guo, J. Xia, B. J. Kirby, P. Shafer, E. Arenholz, H. Chen, X. Zhai, Y. Lu, Correlation-driven eightfold magnetic anisotropy in a two-dimensional oxide monolayer. *Sci. Adv.* **6**, eaay0114 (2020).

Science Advances

Correlation-driven eightfold magnetic anisotropy in a two-dimensional oxide monolayer

Zhangzhang Cui, Alexander J. Grutter, Hua Zhou, Hui Cao, Yongqi Dong, Dustin A. Gilbert, Jingyuan Wang, Yi-Sheng Liu, Jiaji Ma, Zhenpeng Hu, Jinghua Guo, Jing Xia, Brian J. Kirby, Padraic Shafer, Elke Arenholz, Hanghui Chen, Xiaofang Zhai and Yalin Lu

Sci Adv **6** (15), eaay0114.
DOI: 10.1126/sciadv.aay0114